

# A low Z linac and flat panel imager: comparison with the conventional imaging approach

DA Roberts<sup>1</sup>, VN Hansen<sup>1</sup>, AC Niven<sup>2</sup>, MG Thompson<sup>2</sup>, J Seco<sup>3</sup>, PM Evans<sup>1</sup>

<sup>1</sup>Joint Department of Physics, The Institute of Cancer Research and The Royal Marsden NHS Foundation Trust, Downs Road, Sutton, Surrey, UK

<sup>2</sup>Elekta Ltd, Crawley, West Sussex, UK

<sup>3</sup>Massachusetts General Hospital, Harvard Medical, Boston, USA

## Abstract

Experimental and Monte Carlo simulations were conducted of an Elekta Ltd Precise Treatment System Linac fitted with a low Z insert of sufficient thickness to remove all primary electrons. A variety of amorphous silicon based panels employing different scintillators were modelled to determine their response to a variety of x-ray spectra and produce an optimised portal imaging system. This study has shown that in a low Z configuration the vast majority of x-rays are produced in the nickel electron window and with a combination of a carbon insert and caesium iodide based XVI-panel, significant improvement in the object contrast was achieved. For thin, head and neck type geometries, contrast is 4.62 times greater for 1.6cm bone in 5.8cm water than the standard 6MV/iViewGT system. For thicker, pelvis type geometries contrast increases by a factor of 1.3 for 1.6cm bone in 25.8cm water. To obtain images with the same signal to noise ratio as the 6MV/iViewGT system, dose reductions of a factor of 15 and 4.2 are possible for 5.8cm and 25.8cm phantoms respectively. This design has the advantage of being easily implemented on a standard linac and provides a portal image directly from the therapy beam aperture.

## 1. Introduction

Successful treatment of cancer with radiotherapy requires a large radiation dose to be deposited accurately in both position and intensity. To verify that the patient is in the correct position portal images have traditionally been acquired throughout the patient's treatment. Unfortunately these images, produced using the megavoltage treatment beam suffer from inherently low contrast. This in turn limits the ability to position the patient accurately. An increase in accuracy could potentially lead to higher tumour control and/or lower normal tissue complication with the expectation of improved therapeutic benefit.

Several methods for improving this situation have been proposed and fall into three categories. The first method involves changing the object properties, for example by inserting fiducial markers in the treatment region (Dehnad et al. 2003, Nederveen et al. 2003). Secondly, improvements to the imaging device can be made, and thirdly the imaging beam spectrum may be modified. The latter either involves attaching a kV source to the linac (Jaffray et al. 2002), integrating a kV source in the linac (Cho & Munro 2002) or introducing lower atomic number (Z) targets (Cho & Munro 2002, Flampouri et al. 2002, Galbraith 1989, Jabbari et al. 2007, Ostapiak 1998, Tsechanski 1998) into a standard linac. In the last three cases the aim is to produce an imaging spectrum with a high proportion of photons between the energies of 40 and 200 keV. At these energies the photo-electric interaction dominates, and thus bone and soft-tissue contrast is increased compared to the standard MV images where Compton scatter dominates.

In this work we consider using low Z targets in the linac. In previous work substantial contrast improvements have been noted for anthropomorphic phantoms, quantitative measurements utilizing contrast phantoms and even patient images (Flampouri et al. 2005). All aforementioned papers reported a significant improvement in image contrast over the standard portal images used today. They all consider using thin, low Z targets with electron

energies as low as reasonably achievable on the current generation of radiotherapy linacs. This arrangement results in bremsstrahlung production with a significantly lower average energy than the treatment beam. The use of a thin, high Z detector, often with film, was also used to image the lower energy section of the linac spectrum.

Optimisation of such a system differs across the literature. Galbraith (1989) primarily used experimental techniques to produce high contrast images of thin objects using a low Z target thick enough to stop all primary electrons. The images were acquired using film sensitive to energies in the diagnostic range. Ostapiak et al. (1998) and Tsechanski et al. (1998) investigated adjusting the thickness and composition of targets using Monte Carlo methods. They did not however investigate the full imaging system with Monte Carlo methods as in Flampouri et al. (2002). Flampouri et al. (2002) deduced the optimal target to be 6mm of aluminium whilst Tsechanski et al. (1998) used 1.5mm of copper. All the previous studies differ in the way the system was implemented. Of particular note is that different linac types and models were used in each study, which subsequently affected the positioning of the low Z target. Galbraith (1989) and Ostapiak et al. (1998) placed their targets as close to the electron window as possible, whilst Flampouri et al. (2002) and Tsechanski et al. (1998) placed the targets in the secondary filter carousel. This placement is likely to be an important factor in obtaining a high resolution, high contrast image but all authors reported high resolution images.

Firstly it is this discrepancy that we investigate in this paper. It is expected that the electron spot would significantly increase between the vacuum window and any external target, particularly if the target is located approximately 15cm away in the case of Flampouri et al. (2002). It is therefore hypothesised that there is more than one source of photons in a low Z linac and that this source is the electron/vacuum window. In the work by Galbraith (1989) the cross hairs of an AECL Therac-20 were imaged using only photons generated in the aluminium vacuum window. No estimate of the proportions of the photon fluence from the window was noted when a low Z target was placed in the beam. Secondly we have developed an optimum design for a low Z linac given that the target should be placed as close as possible to the vacuum window without a major re-design of the linac head. Thirdly we investigate and model the use of flat panel imagers with the low Z system and assess whether changing the scintillator of the imager has a significant effect on image contrast.

## 2. Apparatus

Both Monte Carlo and experimental techniques were used to investigate the low Z linac and determine an optimized design. Monte Carlo techniques were initially used to investigate the production of photons in a low Z linac and predict image quality with such an imaging system. Experimental results were then obtained to verify the Monte Carlo predictions.

### 2.1 Monte Carlo codes

The EGSnrc based Monte Carlo user codes BEAMnrc (Rogers et al. 1995), DOSXYZnrc\_phsp (Jarry & Verhaegen 2005) and DOSXYZnrc (Walters et al 2004) were used to model an Elekta Ltd Precise Treatment System Linac, a contrast phantom and a variety of amorphous silicon based panels. These models were used to investigate the production of low energy photons in the low Z linac, investigate the photon source size and predict contrast for various phantom and detector combinations. These predictions were compared with experiment.

### 2.2 Linac

An Elekta Ltd Precise treatment system linac (Elekta Ltd, Crawley, UK) was modified by placing a low Z insert into the high energy collimator port. The insert consisted of 2cm of carbon (density=1.8g.cm<sup>-3</sup>) supported by an aluminium alloy cone that fixed to the high energy difference filter mountings on the bottom of the primary collimator. The thickness of the carbon insert was sufficient to stop all primary electrons emerging from the electron window. The carbon insert was placed in the primary collimator as this was the closest position the target could be placed to the exit window of the wave-guide.

The linac was operated in 4MeV electron mode with the primary and secondary scatter foils removed. The only items in the beam path were the nickel electron window, carbon insert, monitor ion chamber, mirror and Mylar cross hair sheet. To increase the dose rate from the linac the electron gun current was increased to match the current used in the high dose rate electron (HDRE) mode of the linac. This increases the beam current by a factor of 10, enabling images to be acquired in clinically acceptable times (circa 1 second). This beam current was used as linacs of this model had previously been life tested to this level. A schematic diagram of the top section of the linac (excluding Jaws and Multi-leaf collimator) can be seen in figure 1.

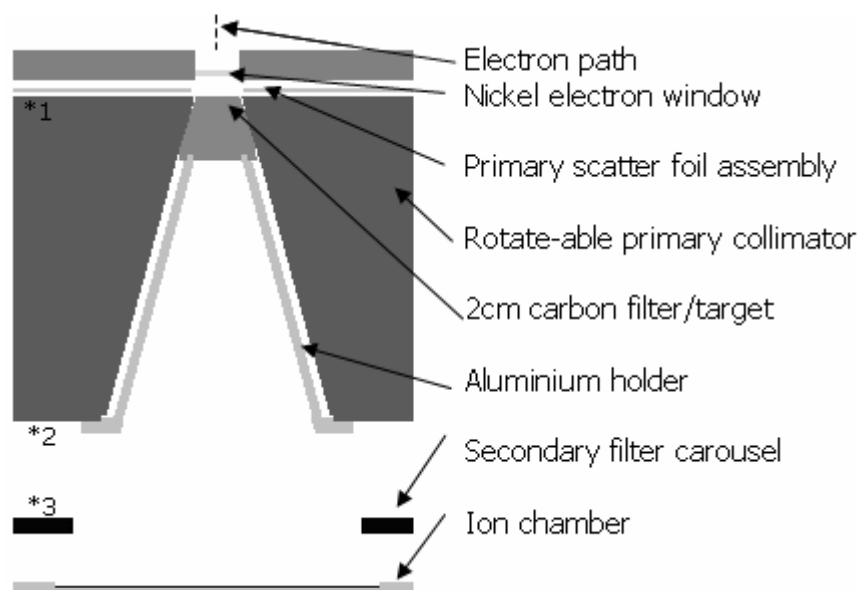


**Figure 1.** Schematic diagram of the top section of the low Z setup. The primary scatter foil assembly is at the hole/photon position and the secondary filter carousel is empty. \*1, \*2, \*3 are the location of phase space files used in the Monte Carlo model.

### 2.3 Phantoms

A tissue-equivalent phantom, Atlantis (Flampouri et al. 2002), shown in figure 2 was used as a quantitative measure of contrast of the different x-ray systems. The phantom consists of varying thicknesses of bone equivalent plastic surrounded by water. Three water depths were used; 5.8, 15.8 and 25.8cm, so as to estimate contrast in the head and neck, torso, and pelvis respectively. The water depths are made up of 0.8cm Perspex (density=1.03g.cm<sup>-3</sup>) and the remainder is water e.g. 5.8cm=5cm water+0.8cm Perspex.

The spatial resolution of the system was assessed by analysing a PIPS pro phantom (Rajapakshe 1996) and images acquired of a humanoid anthropomorphic phantom for the head and neck for qualitative image assessment.

### 2.4 Detectors

Two in-direct amorphous silicon based detectors (Antonuk 2002) manufactured by PerkinElmer (Fremont, California, USA) were considered here. The Elekta iViewGT electronic portal imager (EPID) and the Elekta XVI panel were considered. The major difference between the XVI panel and the iViewGT panel is the omission of the copper plate and the substitution of the gadolinium oxide scintillator for a columnar, thallium doped, Caesium Iodide (CsI (Th)) crystal. The iViewGT panel is normally used for imaging the megavoltage linac beam and the XVI panel is currently used on the Elekta Synergy system for imaging with kV photons.

All panels were positioned in the standard megavoltage detector arm, resulting in a distance of 159cm from the target to the panel surface. Images were acquired using the PerkinElmer x-ray imaging software (XIS) and the panels ran in free running mode i.e. not synchronized to the beam delivery. The iViewGT panel acquired images at 568ms and the XVI panel at 142.5ms. Both frame rates were chosen to avoid saturating the detectors during open field acquisitions but to also give good dynamic range. All images were offset and gain corrected using equation 1 on a pixel by pixel basis.  $I_{corrected}$  is the gain and offset corrected image,  $I_{measured}$  is the image to be corrected,  $I_{gain}$  is a 26x26cm open field image and  $I_{offset}$  is an image acquired when the panel is not being irradiated.

$$I_{corrected}(x, y) = \frac{I_{measured}(x, y) - I_{offset}(x, y)}{I_{gain}(x, y) - I_{offset}(x, y)} \quad (1)$$

## 3. Methods

Initially the hypothesis that photons originated from the electron window was tested using Monte Carlo techniques and a subsequent design for a low Z beam was then determined. The low Z insert was to act as both an electron absorber and target, and thus was placed as close to the electron window as physically possible given the hypothesis that the electrons will spread significantly in air. Image quality parameters, including image contrast and source size were then investigated in conjunction with experimental verification of the system. Dose estimates for image acquisition were also performed experimentally.

### 3.1 Determining the place of origin of the low Z linac photons

**3.1.1 Monte Carlo model commissioning.** Both the 6MV and the low Z beams were modelled. A previously commissioned model of the 6MV beam was used (Parent et al. 2006) whilst the low Z model was commissioned by analysing depth dose curves and profiles of a 4MeV electron beam with no scattering foils and no applicator.

The 4MeV electron beam was used for commissioning the electron energy as electron depth dose curves are more sensitive to electron energy than a photon depth dose. The scattering foils were also removed as this reduced the need to adjust the scattering foil thickness in the calculation to take into account the associated tolerances to obtain a good match with experiment (Faddegon et al. 2008). Commissioning involved simulation of a variety of mono-energetic electron beams impinging on a model of a 4MeV linac setup and the various depth dose curves resulting from them. An optimisation was then performed to determine the optimum truncated Gaussian energy spectrum to match the depth dose curves of the actual 4MeV beam. A truncated Gaussian was chosen as it was assumed the electrons would have a Gaussian-like energy distribution after acceleration and that this distribution would be truncated by the achromatic 112° SLALOM bending magnet system. An arbitrary energy window width was used to match the experimental data. For the 6MV system a circular mono-energetic electron beam of energy 6.2MeV and radius 0.5mm was used. For the low Z system the energy distribution was a truncated Gaussian with a mean of 5.6MeV, a full width at half maximum (FWHM) of 1.9MeV and lower and upper limits of 3.8 and 6.2MeV respectively. The spatial distribution was a circle of radius 0.5mm.

### *3.1.2 - Origin of photons in low Z linac*

Electron source size investigations were conducted by acquiring phase space files at three locations in the scatter foil free linac model. These were calculated at the target and patient sides of the primary collimator and above the secondary filter carousel as shown in figure 1.

The place of production of low energy photons in the low Z linac was determined by tracing the histories of secondary particles in the linac. Using the LATCH (Rogers et al. 1996) feature of BEAMnrc each particles journey through the linac model was tracked. Analysis of a phase space file at the exit of the linac (SSD=100cm) then allowed the particle fluence to be categorised depending on where the particles were produced.

## *3.2 Low Z linac characterisation and imaging experiments*

*3.2.1 Characterising the Low Z linac.* The Low Z linac was characterized by obtaining depth dose curves and profiles in a water tank (Scanditronix-Wellhofer) using a CU500E controller unit and electrometer. The field and reference chambers were compact cylindrical ion chambers, type CC13 with a 0.13cc sensitive volume (Scanditronix-Wellhofer).

Depth dose curves and profiles were acquired for a 20x20cm field, SSD=95cm for both the 6MV and low Z beam using both Monte Carlo and experimental measurements.

*3.2.2 Detector modelling.* The two detectors described previously were modelled using DOSXYZnrc. A previously published model of the iViewGT panel was used (Parent et al. 2006). This was modified for the XVI panel i.e. removal of copper plate and modification of scintillator type and thickness. The image was taken as the dose deposited in the scintillator. Optical photon transport was not included as it was not expected to affect image properties in this case (Evans et al. 2006).

To investigate the response of the panels to various input x-ray spectra the dose deposited in the scintillator layer of the detectors was simulated for various mono-energetic pencil beams. These beams were evenly spaced on a log10 scale between 0.001MeV and 10MeV so as to sample adequately the response of the detectors over the range of energies in question.

*3.2.3 Inherent contrast.* Inherent contrast was assessed using the setup shown in figure 2 both by Monte Carlo calculation and experimental measurement.

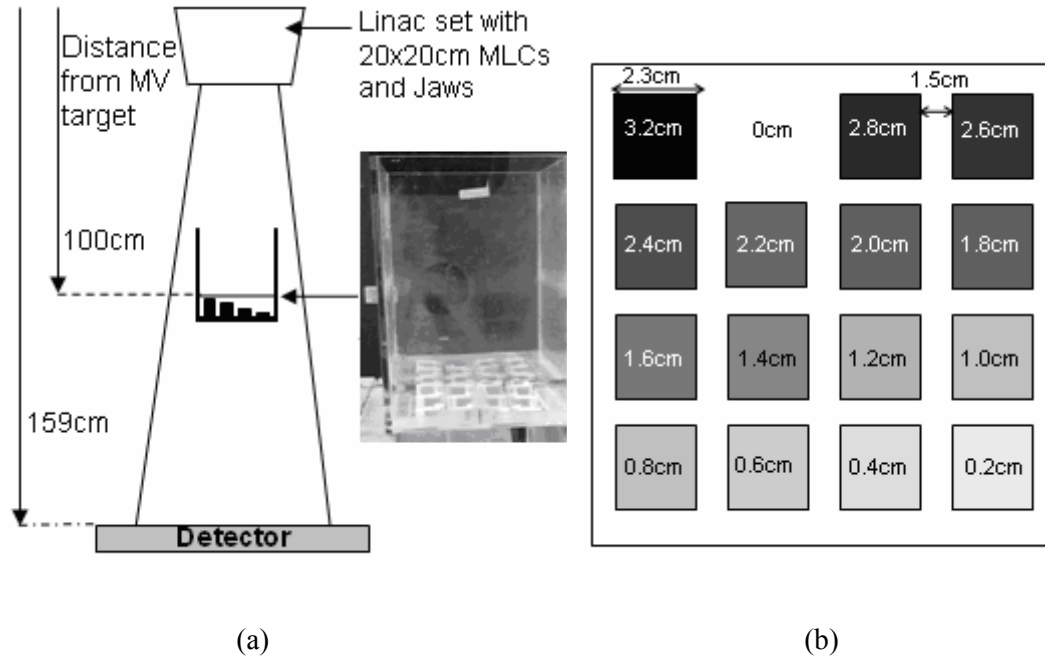


**Figure 2.** (a) Experimental setup for the contrast measurements and (b) schematic diagram of the Atlantis phantom from the top. The Atlantis phantom can be filled to 5.8, 15.8 and 25.8cm water level to simulate various anatomical sites.

The contrast was calculated by analysing the average pixel value in each of the bone segments and using equation 2.  $I_{0\text{cmbone}}$  is the average pixel intensity in the section of the Atlantis phantom with no bone insert (0cm) and  $I_{x\text{cmbone}}$  is the average pixel intensity in the section of the Atlantis phantom with an xcm bone insert. To negate errors associated with a tilted beam and to account for the un-flattened nature of the low Z beam, images of the Atlantis phantom were 'flattened' by dividing this image by one of the same water thickness but without the bone inserts.

$$\text{Contrast}_{x\text{cmbone}} = \frac{I_{0\text{cmbone}} - I_{x\text{cmbone}}}{0.5 * (I_{0\text{cmbone}} + I_{x\text{cmbone}})} \quad (2)$$

**3.2.4 Imaging Dose.** Dose required to form an image was determined two ways: by calculating the dose needed to produce an image with the same signal to noise (SNR) for the low Z system as a standard 2 monitor unit (MU) (~2cGy) 6MV image and the dose required to obtain the same contrast to noise ratio (CNR).

The calibration factor (dose per monitor unit) was determined for the low Z beam. This was determined by placing a farmer chamber at 5cm deep in a solid water phantom measuring 40x40x30cm. The phantom was located at SSD=95cm and a 10x10cm field was used. The dose to the ion chamber was pressure and temperature, ion recombination, and polarity corrected. The dose was also corrected back to dose maximum ( $d_{\text{max}}$ ) for the low Z beam using a previously acquired depth dose curve. The calibration factor for the 6MV and low Z systems was 1.0 cGy/MU and 0.473 cGy/MU respectively.

To investigate the imaging dose for various anatomical sites, movie loops of 5.8, 15.8 and 25.8cm deep water phantoms were acquired. The movie loops allowed us to acquire a sequence of images which were combined to obtain images of a range of dose and SNR levels. To obtain a range of dose levels for the 6MV beam it was run at 37MU/min and the low Z beam ran at its maximum dose rate of 48MU/min. All sequences were acquired after the beams had been on and stabilized for 10 seconds and were running at a constant dose rate.

This allowed us to calculate the number of monitor units per frame, and hence the dose delivered in individual images. The images were gain corrected (equation 1) using flood field movies with the same method. This meant that the gain images were acquired with the same dose as the water phantom images.

Synchronisation artefacts (horizontal line artefacts) were present in both the 6MV and low Z images, and if left un-corrected would adversely affect the image dose calculations. The centre 100x100 pixels were therefore row and column averaged using equation 3 to remove the synchronisation lines and any remaining fixed pattern noise. The same method was used for the 6MV and low Z beam allowing a fair comparison of the two systems.  $I(x,y)$  is the pixel value at position  $(x,y)$ ,  $\bar{J}$  is the mean of the J array produced by finding the mean of every row,  $j_y$  is the pixel value in row  $y$  in array J,  $\bar{K}$  is the mean of the K array produced by finding the mean of every column and  $k_x$  is the pixel value in column  $x$  in array K.

$$I(x,y)_{corrected} = I(x,y) * \left( \frac{\bar{J}}{j_y} * \frac{\bar{K}}{k_x} \right) \quad (3)$$

After correction the SNR was calculated by analysing the same 100x100 pixels using equation 4.  $\bar{I}$  is the mean of the pixel intensities in the centre 100x100 pixels and  $\sigma$  is the standard deviation of the pixels in the centre 100x100 pixels.

$$SNR = \frac{\bar{I}}{\sigma} \quad (4)$$

The SNR data were derived using the water phantom movies. The goal of deriving CNR was to determine CNR as a function of bone thickness  $x$  (in this work a thickness of 1.6 cm was taken). As the water phantom movies did not contain bone inserts, it was necessary to estimate the difference in signal between regions with differing bone thickness using the flattened images of the Atlantis phantom and scale the pixel intensities to the values expected if taken under the same conditions as the water phantom data. This was achieved using equation 5, where equation 5I describes the CNR estimated under the condition of the water phantom measurements, and  $\sigma_{0cm}$  and  $\bar{I}_{0cm}$  were measured directly and  $\bar{I}_{xcm}$  was estimated using scaling deduced from the Atlantis images (equation 5II, where  $\bar{I}_{0cm}^{At}$  and  $\bar{I}_{xcm}^{At}$  were measured in a region from the flattened Atlantis image.). This gave equation 5III to determine the CNR value. This was not done solely using the flattened Atlantis phantom data, as the flattening involves dividing by another image which will increase the noise in the data.  $\sigma_{0cm}$  and  $\bar{I}_{0cm}$  were calculated over the central 100x100 pixels.

$$CNR = \frac{\bar{I}_{0cm} - \bar{I}_{xcm}}{\sigma_{0cm}} \quad (5) \quad I$$

$$\frac{\bar{I}_{xcm}}{\bar{I}_{0cm}} = \frac{\bar{I}_{xcm}^{At}}{\bar{I}_{0cm}^{At}} \quad II$$

III

$$CNR = \frac{\bar{I}_{0cm} (\bar{I}_{xcm}^{At} - \bar{I}_{0cm}^{At})}{\bar{I}_{0cm}^{At} \cdot \sigma_{0cm}}$$

3.2.5 – *Source Size, Spatial resolution and phantom images.* Monte Carlo simulations were used to investigate the photon spot size of the 6MV and low Z linac. A photons last point of interaction was recorded using the “Score Last Z – x, y, z of last interaction” facility of BEAMnrc. Based on the z position of interaction the spot size could be categorized by component module i.e. electron window or carbon insert. This method effectively simulated the experimental technique of Lutz to determine the spot size of radiotherapy linacs (Lutz et al. 1988).

The relative modulation transfer function (RMTF) was calculated from the line pair sections of the PIPS pro phantom as described by Rjapakshe 1996. The images were acquired with the phantom located on a couch at 105.8cm so that the RMTF would contain effects from both the source size and detector resolution.

Images of a head and neck anthropomorphic phantom were acquired to qualitatively observe the image quality of the different x-rays systems. Due to synchronisation artefacts in the images they were row averaged to remove the horizontal banding.

## 4 – Results

### 4.1 - Source of Low Energy Photons

Figure 3a shows Monte Carlo calculation of the electron energy fluence at various levels in a linac for 4MeV electrons.

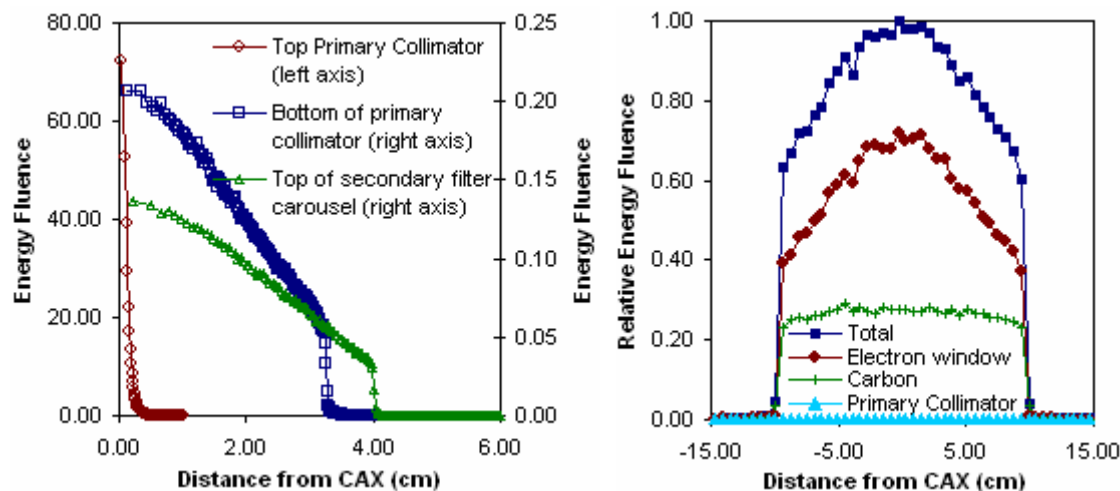


**Figure 3.** (a) Electron energy fluence at various stages of the low Z linac and (b) Photon energy fluence components at SSD=100cm for the low Z linac with a 20x20cm field.

It is shown that the electrons scatter substantially in air between the electron window and the secondary filter carousel. The electron fluence distribution is 8cm wide at the secondary filter carousel and thus any image formed with a target at this level would suffer severe spatial resolution degradation. Therefore to obtain high resolution images a target cannot be placed far from the vacuum window.

The Monte Carlo model of the low Z linac show a substantial photon fluence from the Nickel electron window. Figure 3b shows that at the isocentre plane the majority of the photon fluence is from primary photons produced in the nickel window. In the central 5x5cm of a 20x20cm field 70.95% of the energy fluence is from the electron window, 0.7% from the primary collimator, 28.23% from the carbon insert and 0.12% from other components of the linac. This result explains why high resolution images were acquired by Flampouri et al. (2002) despite the low Z target being placed in the secondary filter carousel where the electron spot size is 8cm wide (figure 3a).

Galbraith 1989 formed images using photons produced from an aluminium electron window in an AECL Therac-20 accelerator, but the contribution from such photons was not discussed in subsequent low Z papers (Flampouri et al. 2002, Ostapiak et al. 1998, Tsechanski 1998). The production of a significant photon fluence in the thin nickel window arises due to nickel's high atomic number ( $Z=28$ ) and density ( $8.9\text{g}\cdot\text{cm}^{-3}$ ). As bremsstrahlung production is proportional to  $Z^2$  the efficiency of the process is greatly increased for the high Z, nickel window over the low Z, carbon insert.

As hypothesized these results show that the vast majority of photons do not come from a low Z target placed inside the linac. In our design the Carbon insert acts to remove primary electrons from the beam and produce further low energy bremsstrahlung photons. It must be noted that the proportion of photons from the electron window will depend on the type of the linac used due to a variety of different materials and thicknesses being used by the linac manufacturers.

#### 4.2 – Depth dose curves and profiles

Figure 4a and b show the depth dose curves and profiles for the low Z beam for the Monte Carlo simulations and experiment. Good agreement is seen between the Monte Carlo and experimental results suggesting that we are correctly modelling the system. A slight tilt in the experimental beam is present as shown in figure 4b and this is likely due to a small tilt in the carbon insert or due to the non-standard operating mode of the ion chamber and servo system. The latter is affected by the lack of secondary electrons normally generated in the flattening filter. This results in a lack of electronic equilibrium in the ion chamber. 6MV data is also shown highlighting the different dosimetric properties of the beams. For 20x20cm fields the 6MV beam  $d_{max}$  is at 1.4cm whilst it is 1.15cm for the Low Z beam.

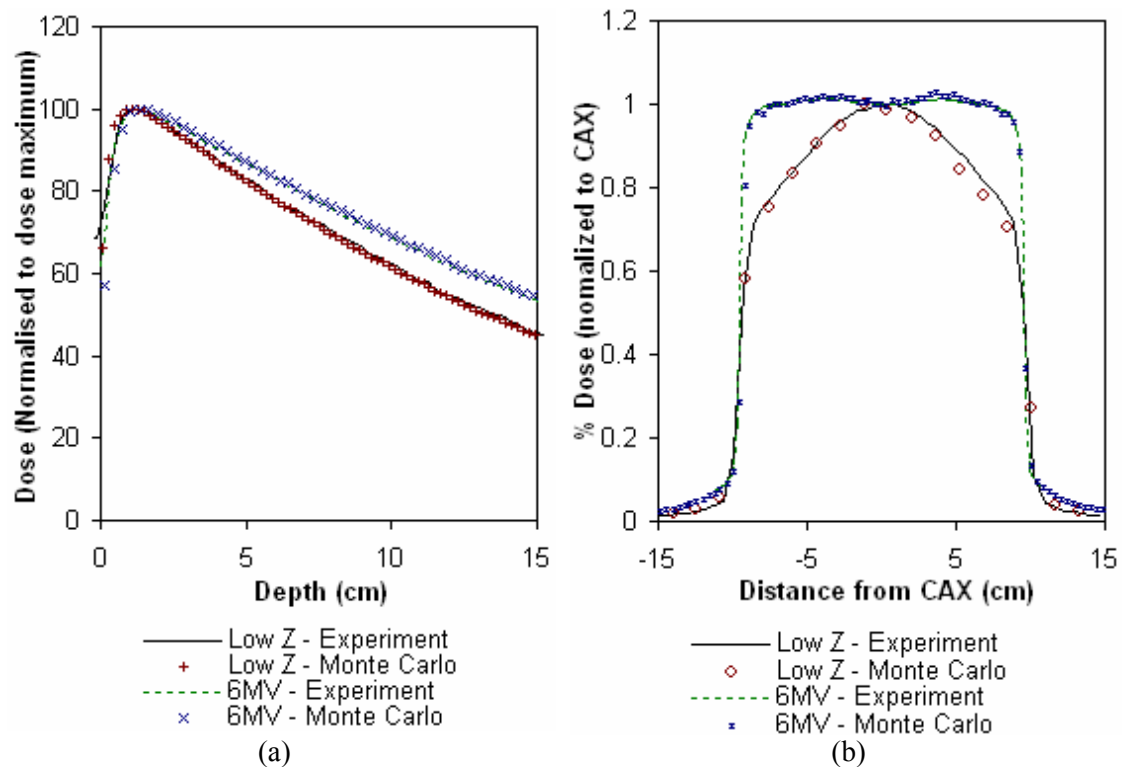


**Figure 4.** (a) Depth dose curves for the low Z and 6MV Beam for a 20x20cm field (b) Profiles at 1cm deep, SSD=95cm for the low Z beam with a 20x20cm field size.

The  $TPR_{10}^{20}$  for a 10x10cm field was 0.665 for 6MV and 0.601 for the low Z beam.

#### 4.3 - Contrast Results

Inherent contrast results calculated for the Atlantis phantom are shown in Figure 5.

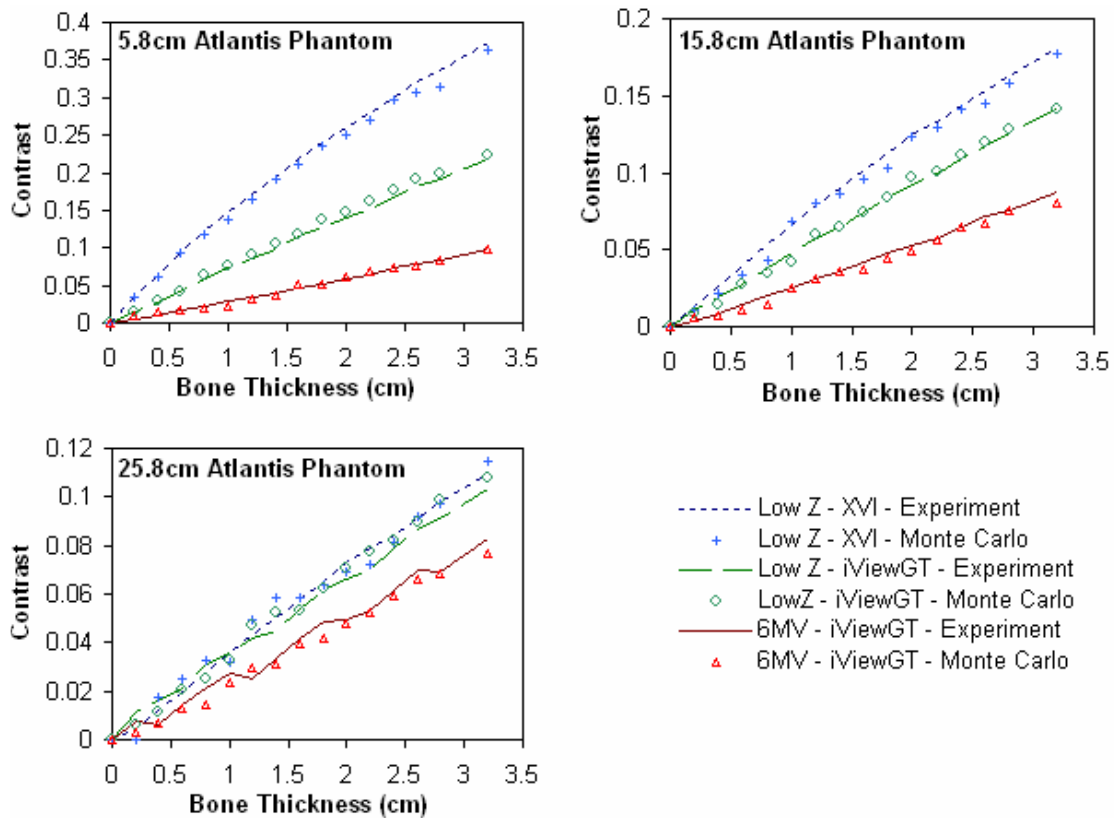


**Figure 5.** Inherent contrast for the LowZ/XVI and 6MV/iViewGT combinations.

Significant improvements in contrast are seen for all low Z beam systems over the standard 6MV/iViewGT system. For thin, 5.8cm phantoms contrast for 1.6cm bone increases by a factor of 2.42 with the LowZ/iViewGT system and by a factor of 4.62 with the LowZ/XVI setup. For thicker phantoms the improvement in contrast decreases but even with a 25.8cm phantom a 1.3 times increase in contrast is noted with the low Z beam. The increase in contrast is due to two factors. Firstly the low Z linac produces a higher proportion of diagnostic x-rays than the 6MV linac and secondly that the different panels are sensitive to different regions of the photon spectrum. Figure 6 illustrates the response of the different detectors as well as the different photon spectra produced by the low Z and 6MV linacs.

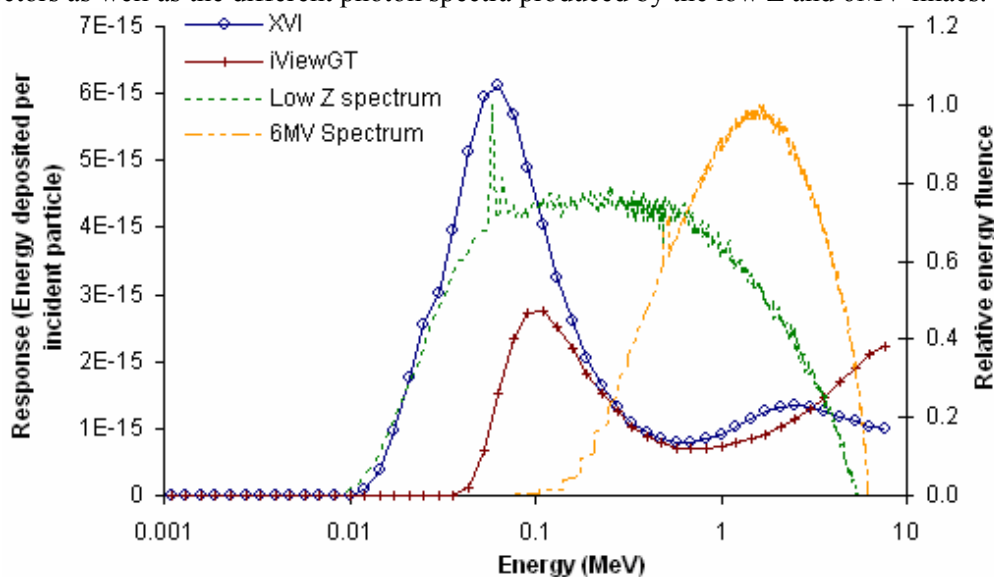


**Figure 6.** Response curves for the XVI and iViewGT panels and photon spectra for the 6MV and low Z beams.

At energies around the mean of the 6MV beam (1.6MeV) the response of all detectors is very low whilst there are very few photons around 100keV for the 6MV beam. Conversely the un-attenuated low Z beam has its peak fluence at or around the maximum response of the detectors. The Elekta iViewGT is less responsive than the XVI panel owing to the thinner and hence less quantum efficient scintillator. The copper plate also limits the quantity of low energy photons that reach the scintillator.

Due to the megavoltage nature of the low Z beam significant beam hardening occurs for thick phantoms. As the phantoms get thicker the beams are stripped of the low energy photons resulting in lower contrast images. The observation of very little contrast improvement for thicker phantoms has been noted previously (Flampouri et al. 2002, Galbraith 1989, Ostapiak 1998, Tsechanski 1998) and remains one of the disadvantages of any megavoltage generated low Z beam.

#### 4.4 – Imaging Dose

Table 1 presents the dose needed to form an image with the same Signal to noise ratio as the conventional 6MV/iViewGT system. Table 2 shows the imaging dose required to form an image with the same Contrast to Noise Ratio (CNR).

**Table 1.** Dose comparison for the low Z/XVI system when the SNR is kept the same as the standard 6MV/iViewGT system.

Phantom	Beam	SNR	Dose	% of 6MV Dose	Contrast <sup>1</sup>
5.8cm Water	6MV/iViewGT	96.35	2cGy	100%	0.0474
	LowZ/XVI	96.35	0.13cGy	6.63%	0.2190
25.8cm Water	6MV/iViewGT	68.89	2cGy	100%	0.0426
	LowZ/XVI	68.89	0.48cGy	24%	0.0575

<sup>1</sup> Contrast value for 1.6cm Bone in x cm water

**Table 2.** Dose comparison at a constant contrast to noise ratio.

Phantom	Beam	CNR <sup>1</sup>	Dose	% of 6MV Dose
5.8cm Water	6MV/iViewGT	21.39	2cGy	100%
	LowZ/XVI	21.39	0.009cGy	0.45%
25.8cm Water	6MV/iViewGT	8.37	2cGy	100%
	LowZ/XVI	8.37	0.272cGy	13.6%

<sup>1</sup> CNR value for 1.6cm Bone in x cm water

Both sets of results show a significant dose saving for thin phantoms. A dose reduction of a factor of 15 is possible for a 5.8cm phantom whilst still obtaining a 4.62 times increase in contrast. For the thickest phantom a dose saving of a factor of 4.2 and an increase in contrast of a factor of 1.3 is observed. Contrast to noise ratio calculations show that a further reduction in dose is possible for constant CNR. 0.45% of the dose is required for thin phantoms for the low Z beam compared to the 6MV system. For thicker phantoms we require 13.6% of the dose of the 6MV images for the Low Z system.

Imaging times vary according to the phantom thickness due to the restricted beam current used for the low Z beam to safeguard the electron window. For a 5.8cm phantom, images with the same SNR as a 2cGy 6MV image can be acquired in 0.35 seconds. For a 25.8cm phantom this increases to 1.27 seconds. These times are acceptable for portal imaging but if quicker acquisitions were required for cone beam CT then the SNR would have to be sacrificed or a thicker scintillator with a high quantum efficiency (QE) employed.

#### 4.5 – Spatial Resolution

The photon source of the low Z linac is a combination of photons emitted from the electron window and Carbon insert as shown in Figure 7. For both the 6MV and low Z Monte Carlo simulations, the input electron spot size was the same. However due to the different positions of the targets the overall photon spot shape is slightly different. The 50% points are similar for the two systems but the Low Z beam has a broader tail around the 15% region. The broadening of the tails is due to the larger electron spot hitting the Carbon insert after passing through the nickel electron window and being scattered in a volume of air. This could be improved by moving the carbon target/filter closer to the nickel window.

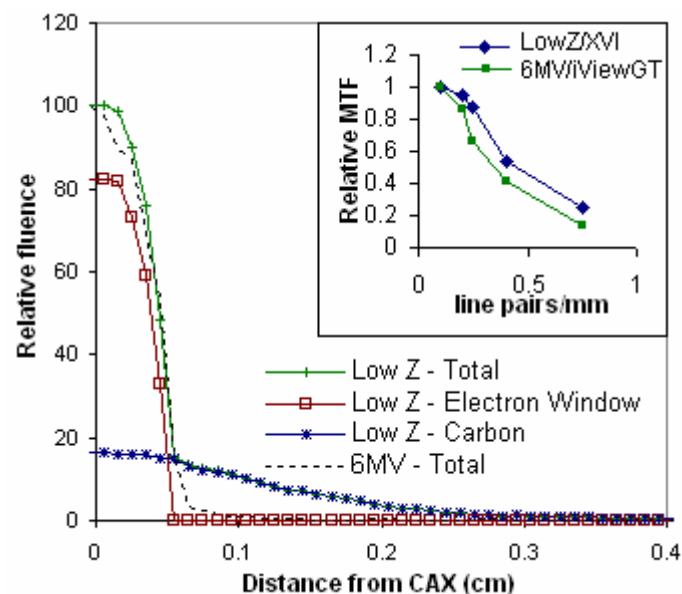
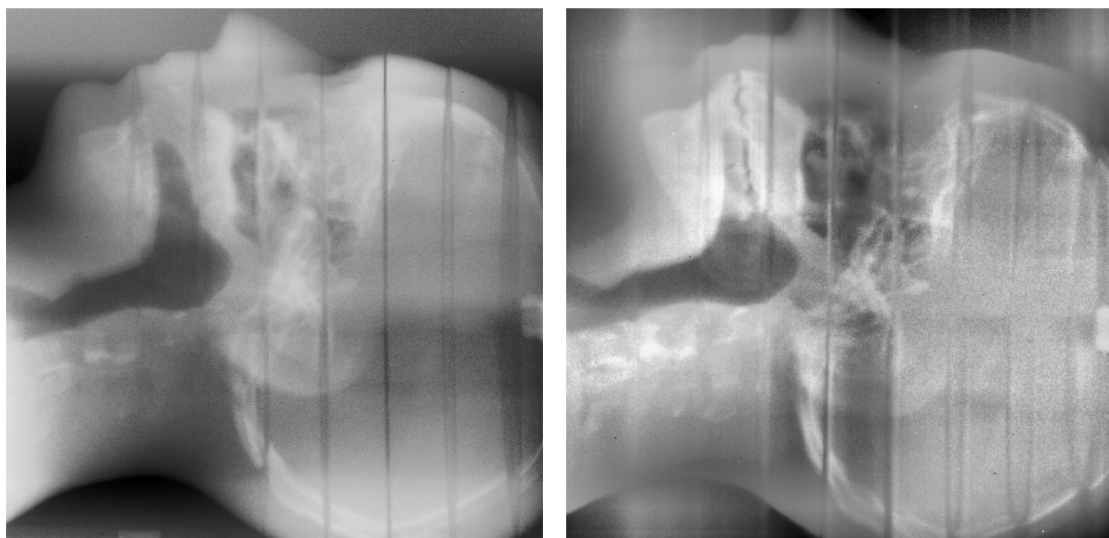


**Figure 7.** Monte Carlo calculated source size for 6MV and low Z setups. The insert shows the MTF results for the 6MV/iViewGT and LowZ/XVI systems.

Spatial resolution of the whole system was assessed by measuring the MTF using the PIPS-pro phantom placed on a couch at SSD=105.8cm. The figure 7 insert shows the MTF's for the LowZ/XVI and 6MV/iViewGT systems. The LowZ/XVI system performs better at higher frequencies resulting in sharper images. Whilst the detectors are similar, the presence of the copper plate on the iViewGT panel increases the size of the point spread function for the 6MV beam by scattering electrons and photons before they interact with the scintillator. Also the higher energy 6MV photons may scatter larger distances and can backscatter into the scintillator. On the other hand the secondary source of photons from the carbon insert in the low Z linac act to reduce the MTF as they broaden the low Z spot size.

#### 4.6 – Qualitative Phantoms

Figure 8 shows a comparison between the current 6MV/iViewGT system and the experimental LowZ/XVI system. The 6MV/iViewGT image was formed with 2cGy and the LowZ/XVI with 0.1623cGy.



(a) (b)  
**Figure 8.** Images of a head and neck phantom for (a) 6MV/iViewGT (2cGy) and (b) Low Z/XVI (0.16cGy) systems. Images have been adaptive histogram equalized.

Image quality is superior in the Low Z/XVI image supporting the quantitative measurements described previously, despite the image being formed with a lower dose. Teeth, oral cavity and spine are clearly visible in the LowZ/XVI image highlighting the superior contrast and preservation of spatial resolution.

## 5. Conclusion

A low Z system has been implemented that produces superior images than that of the current 6MV/iViewGT combination. Use of a highly quantum efficient detector optimized for the kV energy range has resulted in a contrast improvement of a factor of 4.62 for thin (5.8cm thick) phantoms and 1.3 for thicker 25.8cm phantoms. Most importantly significant dose savings have been noted suggesting this technique would be well suited for megavoltage CT. Such systems have been limited by the large dose required to acquire the projection images.

The system offers a very simple modification to a standard linac coupled with a readily available imaging panel. Whilst the system cannot compete with the dose and contrast results of gantry mounted kV systems it offers a less complex solution and an image originating from the therapeutic portal of the linear accelerator.

## Acknowledgements

This work is supported by Elekta Ltd and The Institute of Cancer Research. Work of the radiotherapy physics group is partially supported by Cancer Research UK under programme grant C46/A3970. We are grateful for information provided by Elekta Ltd and Perkin Elmer for the purposes of modelling the linac and detectors. We are extremely grateful to Andrew Lake for helping with the experiments and to Alan Hitchings for advice on the target holder design. Also to Nick Smith, Clive Long and Craig Cummings for manufacturing and modifying the target insert and to Mike Partridge for useful discussions relating to detectors. We would also like to thank all the ICR/RMH physics staff who have contributed with comments or help with this work.

## References

- Antonuk L E 2002 Electronic portal imaging devices: a review and historical perspective of contemporary technologies and research *Physics in Medicine and Biology* **47** R31-R65.
- Cho Y B and Munro P 2002 Kilovision: Thermal modeling of a kilovoltage x-ray source integrated into a medical linear accelerator *Medical Physics* **29** 2101-2108.
- Dehnad H, Nederveen A J, van der Heide U A, van Moorselaar R J A, Hofman P and Legendijk J J W 2003 Clinical feasibility study for the use of implanted gold seeds in the prostate as reliable positioning markers during megavoltage irradiation *Radiotherapy and Oncology* **67** 295-302
- Evans P M, Mosleh-Shirazi M A, Harris E J and Seco J 2006 Monte Carlo and Lambertian light guide models of the light output from scintillation crystals at megavoltage energies *Medical Physics* **33** 1797-1809
- Faddegon B A, Perl J and Asai M 2008 Monte Carlo simulation of large electron fields *Physics in Medicine and Biology* **53** 1497-1510
- Flampouri S, Evans P M, Verhaegen F, Nahum A E, Spezi E and Partridge M 2002 Optimization of accelerator target and detector for portal imaging using Monte Carlo simulation and experiment *Physics in Medicine and Biology* **47** 3331-3349.
- Flampouri S, McNair H A, Donovan E M, Evans P M, Partridge M, Verhaegen F and Nutting C M 2005 Initial patient imaging with an optimised radiotherapy beam for portal imaging *Radiotherapy and Oncology* **76** 63-71
- Galbraith D M 1989 Low-Energy Imaging with High-Energy Bremsstrahlung Beams *Medical Physics* **16** 734-746.
- Jabbari K, Sarfehnia A, Podgorsak E B and Seuntjens J P 2007 Monte Carlo feasibility study of orthogonal bremsstrahlung beams for improved radiation therapy imaging *Physics in Medicine and Biology* **52** 1171-1184
- Jaffray D A, Siewerdsen J H, Wong J W and Martinez A A 2002 Flat-panel cone-beam computed tomography for image-guided radiation therapy *International Journal of Radiation Oncology Biology Physics* **53** 1337-1349
- Jarry G and Verhaegen F 2005 Electron beam treatment verification using measured and Monte Carlo predicted portal images *Physics in Medicine and Biology* **50** 4977-4994
- Lutz W R, Maleki N and Bjarngard B E 1988 Evaluation of A Beam-Spot Camera for Megavoltage X-Rays *Medical Physics* **15** 614-617
- Nederveen A J, Dehnad H, van der Heide U A, van Moorselaar R J A, Hofman P and Legendijk J J W 2003 Comparison of megavoltage position verification for

prostate irradiation based on bony anatomy and implanted fiducials *Radiotherapy and Oncology* **68** 81-88

Ostapiak O Z, O'Brien P F and Faddegon B A 1998 Megavoltage imaging with low Z targets: Implementation and characterization of an investigational system *Medical Physics* **25** 1910-1918

Parent L, Seco J, Evans P M, Fielding A and Dance D R 2006 Monte Carlo modelling of a-Si EPID response: The effect of spectral variations with field size and position *Medical Physics* **33** 4527-4540

Rajapakshe R, Luchka K and Shalev S 1996 A quality control test for electronic portal imaging devices *Medical Physics* **23** 1237-1244

Rogers D W O, Faddegon B A, Ding G X, Ma C M, We J and Mackie T R 1995 Beam - A Monte-Carlo Code to Simulate Radiotherapy Treatment Units *Medical Physics* **22** 503-524

Tsechanski A, Bielajew A F, Faermann S and Krutman Y 1998 A thin target approach for portal imaging in medical accelerators *Physics in Medicine and Biology* **43** 2221-2236.

Walters B, Kawarakow I, & Rogers D W O 2004, *DOSXYZnrc users manual NRCC Report PIRS-794revB* NRCC, Ottawa, Canada.